

Experimental study on gravity currents with internal stratification in semicircular channels

L. Chiapponi

*Department of Engineering and Architecture - Università degli Studi di Parma - Parco
Area delle Scienze 181/A - 43124 Parma, Italy*

T. Zemach

Department of Computer Science, Tel-Hai College, Tel-Hai 1220800, Israel

D. Petrolo

*Department of Engineering and Architecture - Università degli Studi di Parma - Parco
Area delle Scienze 181/A - 43124 Parma, Italy*

M. Ungarish

*Department of Computer Science, Technion, Israel Institute of Technology, Haifa 32000,
Israel*

S. Longo¹

*Department of Engineering and Architecture - Università degli Studi di Parma - Parco
Area delle Scienze 181/A - 43124 Parma, Italy*

Abstract

We present an experimental study of gravity currents (GCs) with internal stratification in a semicircular channel in the inertial–buoyancy and Boussinesq regime. Forty tests were performed with a denser volume of fluid (brine advancing in a fresh water ambient fluid) in lock-release. The lock contains an internal stratification, with a layer of density ρ_L overlain by a layer of density ρ_U , where $\rho_a < \rho_U < \rho_L$ and ρ_a is the density of the ambient fluid. The experiments cover both a full depth and a partial depth configuration. The measurements consist of marking the front position of the currents as

¹Corresponding author

a function of the time from release, t . Two lateral video-cameras were used to detect the flow profile. Also local instantaneous density and velocity profiles data were collected in a fixed section downstream of the gate, in order to give further details and a better description of the physical phenomenon. The integral data of front speed and current thickness were compared to a theoretical model [1] based on (i) a Boussinesq flow; (ii) large Reynolds number; (iii) current advancing in shallow water conditions; and (iv) negligible ambient fluid dynamics. The system of equations and boundary conditions allows the prediction of the motion of the GC, in particular the position and speed of the nose $x_N(t)$ and $u_N(t)$. The agreement of theory and experiments is fairly good, especially for the full depth configuration. The partial depth configuration experiments are less accurately reproduced by the theory, and require a correction coefficient of the Froude number at the front, that accounts for the deviations of the realistic system from the free-slip and sharp non-entraining interface in the control volume about the head.

Keywords: gravity currents, experiments, stratification, shallow water, buoyancy fluxes

1. Introduction

Gravity currents (GCs) develop whenever there are horizontal variations in density in a fluid under the action of a gravitational field. The densities of the current, ρ_c , and of the ambient fluid, ρ_a , can be uniform or “stratified” (i.e., vary with the vertical coordinate z). The current and ambient fluid are not necessarily different, as a difference in density may be related to a difference in temperature or to suspended particles inside the heavier fluid. These currents propagate at the bottom of the ambient fluid when $\rho_c > \rho_a$ (hyperpycnal), or at the top of the ambient fluid in the opposite case (hypopycnal). If the ambient fluid is stratified, currents may propagate at the level of equal density (mesopycnal intrusion). Here we consider a bottom (or dense) current, $\rho_c > \rho_a$.

Many examples of GCs occur in natural and artificial environments, as reported in the exhaustive monographs by Simpson [2] and Huppert [3]. Here we mention only a few: (i) dust and sand risen from turbulent wind (i.e., sandstorms), (ii) the sea breeze, which is the flow of cool moist air from the sea to the land, (iii) the current that flows into a warm house through a

doorway when it is opened on a cold windless day, (iv) the gas and vapour column during volcanos eruptions (see [4]).

GCs can be classified upon the dominant terms that control the momentum balance, so we can distinguish inertial-buoyancy from viscous-buoyancy regimes, or even turbulent drag-buoyancy balance in presence of obstacles or vegetation. A further classification can be made upon the release mechanism at the source: in some cases a finite volume of fluid stored in a reservoir can be instantaneously released in the environment (then we deal with lock-release GC), but in some other cases, the release of the current can be continuous in time at constant or time-varying flow rate. In the modelling of the phenomena, the Boussinesq approximation is often adopted if the current and the ambient fluids have a similar density, i.e. $\rho_a/\rho_c \rightarrow 1$; the one-layer approximation can be adopted when the ambient fluid dynamics is negligible compared to that of the current. Ungarish [5] details these models and the approximations.

During propagation, an initially homogeneous fluid current undergoes a stratification process, because of entrainment of ambient fluid [6], or due to a progressive settling of coarse and then fine particles for sediment-laden fluids[7, 8], or due to explosive decompression by a pressurized dome in volcanic settings that release suspension into the air [9]. Hacker et al. [6] showed that part of the dense fluid is detrained from the nose of the current as a consequence of breaking of Kelvin-Helmholtz waves; this fluid must be replaced by denser fluid propagating forward from the rear of the current, leading to a progressive dilution of the current, with a mixing rate that depends on many factors, like the aspect ratio of the lock. The important role of the Kelvin-Helmholtz instabilities in the GC propagation over a horizontal or inclined bottom, was also studied by Ottolenghi et al. [10, 11], who showed that for low values of the aspect ratio of the lock volume, billows are confined in the body of the current and are more stable, and the entrainment is boosted. Therefore, the scenario of currents that are initially homogeneous and remain so during the propagation process is a simplistic schematisation of a much more complex behaviour.

Some other researchers focussed on GCs which are stratified in their initial condition. Gladstone et al. [12], Dai [13], Wu and Dai [14] studied the influence of a two-layer stratification of the dense current in lock-release experiments with rectangular geometry.

Zemach and Ungarish [15] developed a one-layer shallow water model for

gravity currents with internal stratification and compared the predictions with the available experimental data. It turns out that this simple model reproduces well the main features of the flow: initial slumping phase, then similarity behaviour of the front position of the current x_N , with time t , so that $x_N \propto t^{2/3}$, transition to viscous regime, and stability of the interfaces between the layers of various densities. This is a quite encouraging performance for a self-contained model (without tuning parameters).

All previously mentioned studies focus on channels with a rectangular cross-section. The recent model by Zemach and Ungarish [1] extends the analysis to the case of non-rectangular cross-sections, obtaining self-similar front propagation in channels with cross-sections of power-law shape. We recall that a rectangular cross-section is a simple scheme that allows us to capture many essential aspects of the propagation process; however, a rectangular cross-section is not very frequent in the environment, and even in the case of artificial channels the cross-section is most frequently trapezoidal and circular. From this point of view, the extension of the model to a non-rectangular cross-section has immediate application significance. However, the theoretical extension lacks experimental support. This gap of knowledge motivated the present work. We performed a set of experiments in a circular cross-section channel with internal stratification currents. The experiments cover a fairly wide range of parameters and were compared with the predictions of the shallow water model. This provides an assessment of the accuracy of the predictions, as well as insights into some details not covered by simple model.

The paper is structured as follows. Section 2 shortly recalls the theory and the model, §3 describes the experimental apparatus and §4 the experiments. Section 5 contains the relevant aspects of the activity and the conclusions.

2. Theoretical model for stratified GCs

Here we present the essentials of the theoretical model used in our investigation. This model served a guideline for the design and set-up of the experiments, and it is also used for comparisons with, and interpretation of, the data recorded in our experiments. We note that the model was developed by Zemach and Ungarish [1].

The typical system configuration is sketched in Figure 1. Consider a gravity current created by the release from a lock of a stratified fluid of

density ρ_c into an ambient fluid of density ρ_a and propagating in the x -direction within a horizontal channel of circular cross-section(CS). Gravity acts in the $-z$ -direction.

The current is distributed in two layers of density, i.e., is internally stratified, as follows:

$$\rho_c = \begin{cases} \rho_L, & (0 \leq z \leq h_L), \\ \rho_U, & (h_L < z \leq h), \end{cases} \quad (1)$$

where $h_L = h_L(x, t) \in (0, h)$ and h is the level of the current interface. The density of the ambient fluid, in front and above the propagating current, is $\rho_a = \text{const}$. We assume a stable system $\rho_a < \rho_U < \rho_L$, without stratification of velocity. Also the condition $\rho_a = \rho_U$ can occur, that is the case of a homogeneous GC generated by a partial-depth lock release, not treated in the present work since it was previously studied in Longo et al. [16].

We first introduce the governing parameters and dimensionless numbers of our system. The maximal reduced density difference of the current at the bottom with the ambient is given by:

$$\epsilon = \frac{\rho_L - \rho_a}{\rho_a}. \quad (2)$$

We employ the Boussinesq approximation expressed as $0 < \epsilon \ll 1$, which is relevant in geophysical and environmental applications.

The driving effect is the reduced gravity, defined by

$$g' = \epsilon g, \quad (3)$$

where g is the gravitational acceleration. We emphasize that this g' is a formal value, based on the largest density difference; the presence of stratification is expected to influence the effective buoyancy driving effect as shown later.

As a measure of the importance of the internal stratification, we introduce the parameter σ :

$$\sigma = (\rho_L - \rho_U)/(\rho_L - \rho_a), \quad \text{i.e.,} \quad (\rho_L - \rho_U)/\rho_a = \sigma\epsilon. \quad (4)$$

σ is a given constant in the range $[0, 1]$. $\sigma = 0$ means no internal stratification (the standard homogeneous current); while $\sigma = 1$ means that the density of current matches the density of the ambient at the interface $z = h$.

The geometry of the bottom cross-section is a circle. The width (from left to right boundaries) is given by the function $f(z) = 2\sqrt{2zR - z^2}$, where R is the radius of the circular CS. As a result, the cross-section of the current is given by $A = \int_0^h f(z)dz$ and the total cross-section occupied by the fluid is given by $A_T = \int_0^H f(z)dz$, where H is the height of the container. The areas of the lower and upper layers of the current are correspondingly $A_L = \int_0^{h_L} f(z)dz$ and $A_U = A - A_L$ and the areas ratio is described by the parameter $\Omega = A_L/A$. During propagation both A_L and A change with x, t . However, the initial value of Ω is preserved during the motion and it remains unchanged at any x, t (the proof is given in [1]). Roughly, the layers of density ρ_L and ρ_U elongate like ribbons of same length, $x_N(t)$. Volume conservation of each component is fulfilled when the area ratio is maintained.

The dimensionless parameters are as follows: the x -lengths are scaled by the lock length x_0 ; the vertical z -lengths and the lateral y -lengths are scaled by the initial height of the dense fluid in the lock h_0 . The cross-section areas and volume are thus scaled by h_0^2 and $x_0 h_0^2$ respectively. Inspection of the depth-averaged driving pressure term (see [1]) indicates that the effective reduced gravity at release is $g'[1 - \sigma\gamma(h_0)]$; as expected, the internal stratification reduces the buoyancy driving effect, and this we incorporate in the scaling speed and time. The speed is scaled by U and the time is scaled by T where

$$U = [h_0 g'(1 - \sigma\gamma(h_0))]^{1/2}, \quad T = x_0/U, \quad (5)$$

where

$$\gamma(h) = 1 - \Omega^2 \frac{f(h)}{f(h_L)}, \quad (6)$$

while pressure is scaled with $\rho_a U^2$. We assume a thin-layer buoyancy–inertia (large Reynolds number, see below) flow.

The shallow water approximation provides the governing equations for the position of the interface h measured from the bottom line of the tank and the area-averaged velocity u of the dense fluid as functions of t and x for the cross-section of circular form. In dimensionless form, the volume continuity and momentum equations can be written [1] by

$$\begin{Bmatrix} h_t \\ u_t \end{Bmatrix} + \begin{bmatrix} u & \frac{A(h)}{f(h)} \\ \frac{1 - \sigma\gamma(h)}{1 - \sigma\gamma(1)} & u \end{bmatrix} \begin{Bmatrix} h_x \\ u_x \end{Bmatrix} = \begin{Bmatrix} 0 \\ 0 \end{Bmatrix}. \quad (7)$$

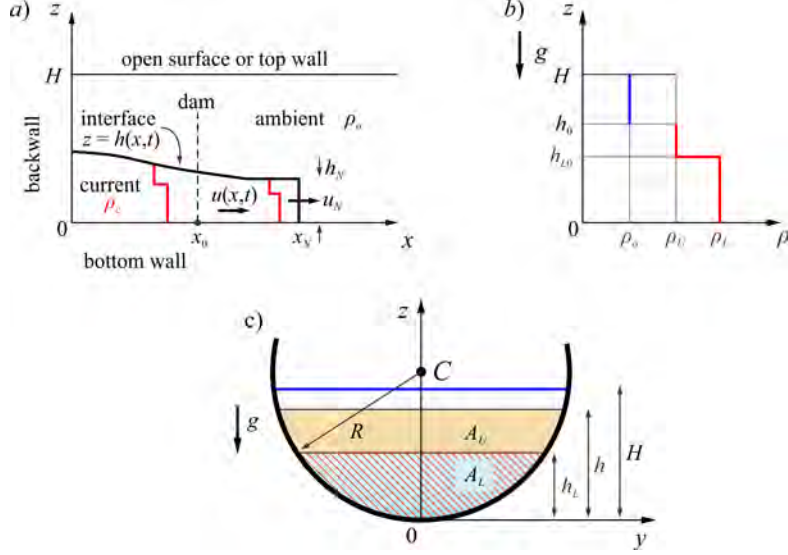


Figure 1: A description of the *a*) lock-release problem, *b*) the density profile, and *c*) the circular cross-section.

The system of partial differential equations (7) is hyperbolic with characteristic relationships and trajectories given by

$$\frac{f(h)}{A(h)} \Gamma(h) \cdot dh \pm du = 0 \quad \text{on} \quad \frac{dx}{dt} = \lambda_{\pm} = u \pm \Gamma(h), \quad (8)$$

where

$$\Gamma(h) = \sqrt{\frac{A(h)}{f(h)} \cdot \frac{1 - \sigma\gamma(h)}{1 - \sigma\gamma(1)}}. \quad (9)$$

The initial conditions in the lock $x \in [0, 1]$ are $h = 1, u = 0$ at $t = 0$, and $x_N(t = 0) = 1$. The boundary conditions are $u = 0$ at $x = 0$; at the nose $x = x_N$ we apply the extension of Benjamin's result to the present flow field,

$$\frac{dx_N}{dt} \equiv u_N = Fr(\varphi_N) \cdot \Psi \cdot h_N^{1/2}, \quad (10)$$

where Ψ is the stratification nose-speed coefficient given by

$$\Psi = \left[\frac{1 - \sigma(1 - h_L/h_N)}{1 - \sigma\gamma(1)} \right]^{1/2} \quad (11)$$

and the ‘‘Froude number’’ Fr is given by:

$$Fr(\varphi) = \left[\frac{2(1-\varphi)^2}{1+\varphi} (1+Q) \right]^{1/2}, \quad (12)$$

where

$$\varphi = \frac{A}{A_T} \quad \text{and} \quad Q = \frac{\int_0^h z f(z) dz}{h \cdot (A_T - A)}. \quad (13)$$

To evaluate the height of the bottom layer h_L , we keep in mind that $\Omega = \text{const.}$ (given by the initial conditions) and employ the relation

$$\frac{\partial h_L}{\partial h} = \Omega \frac{f(h)}{f(h_L)}. \quad (14)$$

Then the upper height h_U can be obtained using $h_U = h - h_L$. The initial condition $h_L(0)$ in the lock is given.

2.1. Time-dependent solutions

We employ a two-step Lax-Wendroff finite-difference method to solve Equation (7) and obtain $h(x, t)$, $u(x, t)$ and $x_N(t)$. The variable domain $[0, x_N]$ is transformed into a fixed domain $[0, 1]$ by mapping the x coordinate into $\eta = x/x_N(t)$. This method was successfully used for the gravity currents in rectangular and non-rectangular channels. The SW results displayed here were obtained with, typically, 200 grid points in the $[1, x_N]$ interval and a time step of $1 \cdot 10^{-3}$. For comparison and further verification, we also integrated the differential problem by employing the method of characteristics along the two trajectories, with choice of time and space step to ensure that the Courant number $U\Delta t/\Delta x < 0.5$, where U is the current velocity and $\Delta x = 1/100$. The formulation above does not contain adjustable constants. We note that the definition of Fr (given in Equation 12) is a strong idealization. This is a theoretical result for a steady-state head with free-slip boundary conditions and sharp interface, an extension of Benjamin’s Fr solution for a 2D flow. In practice (like in our experimental tank) viscous friction and mixing in the head are unavoidable, and a reduction of Fr occurs. This realistic reduction can be expressed by a multiplication of the ideal Fr by a coefficient $\chi \approx 0.8$ (to be used later); in the 2D case, a change from Benjamin’s formula to the semi-empirical Huppert Simpson formula is often used. The incorporation of such a coefficient in the solution, when desired, is straightforward.

2.2. Slumping stage and similarity solution

The prediction of the system (7)–(13) and initial conditions is that after release from rest, the GC enters into a slumping phase of propagation with constant nose height h_N and velocity u_N over a significant distance.

The values of h_N and u_N during the slumping stage can be calculated following a forward-propagating characteristic λ_+ from a point in the unperturbed domain (where $u = 0$ and $h = 1$), to the point where the velocity and the height have the constant values (h_N and u_N) using

$$u_N = \int_1^{h_N} \frac{f(h)}{A(h)} \Gamma(h) dh. \quad (15)$$

The intersection with the nose condition (10) yields an implicit equation for h_N :

$$\int_1^{h_N} \frac{f(h)}{A(h)} \Gamma(h) dh = Fr(\varphi_N) \cdot \Psi \cdot h_N^{1/2} \quad (16)$$

which provides first h_N , and next u_N .

For large times (or rather in asymptotic intermediate conditions, not too early, not too late) a self similar solution is possible only if the CS is a power law $f(z) = bz^\alpha$. In this stage of propagation, the current is already thin and therefore we consider Fr to be a constant and equal to $\sqrt{2}$.

For $R \gg 1$, the circular CS $f(z) = 2\sqrt{2zR - z^2}$ can be approximated by $f(z) = bz^{1/2}$ as follows:

$$f(z) = 2\sqrt{2zR} \cdot \left(1 - \frac{z}{2R}\right)^{1/2} \approx 2\sqrt{2zR} \left(1 - \frac{z}{4R}\right) \approx 2\sqrt{2zR} = bz^{1/2}, \quad (17)$$

where $b = \text{const}$. Also note $\gamma = 1 - \Omega^{2/3}$.

According to Zemach and Ungarish [1] the similarity solution is given by

$$x_N(t) = K(t + \tau)^{3/4}; \quad h(\eta, t) = (\dot{x}_N)^2 \mathcal{H}(\eta); \quad u(\eta, t) = \dot{x}_N \mathcal{U}(\eta), \quad (18)$$

where τ is a time-shift constant and

$$\begin{aligned} \mathcal{H}(\eta) &= \frac{1}{2\Psi^2} - \frac{1 - \eta^2}{6}, \\ \mathcal{U}(\eta) &= \eta, \\ K &= \left(\frac{4}{3}\right)^{3/4} \left(\frac{1}{\int_0^1 \mathcal{H}^{3/2}(\eta) d\eta}\right)^{1/4}, \\ \Psi &= \left[\frac{1 - \sigma(1 - \Omega^{2/3})}{1 - \sigma(1 - \Omega^{5/3})}\right]^{1/2}. \end{aligned} \quad (19)$$

The similarity solution does not satisfy initial conditions and contains an unspecified constant τ . Consequently, this result is relevant only for large t .

2.3. Dimensionless numbers

We define (see Zemach and Ungarish [1]) the Reynolds number (dimensional variables)

$$Re = \frac{Uh_0}{\nu}, \quad (20)$$

where ν is the kinematic viscosity of the current, and the effective Reynolds number (dimensionless variables, see [5]) by

$$Re_e = \left(Re \frac{h_0}{x_0} \right) \frac{u_N h_N^2}{x_N}. \quad (21)$$

During propagation the GC becomes thinner and slower, and hence the ratio of inertia to viscous forces, expressed by (21), changes (actually decreases) with t (or x_N) and can be calculated from the SW finite-difference solution. The position x_N , at which $Re_e = 1$, defines the transition length to the viscous regime. In most of our experiments the flow did not enter into the viscous regime, i.e., the corresponding SW solution predicts $Re_e > 1$ for the time (and distance) of propagation recorded in the laboratory.

In the presence of three densities, some interfacial instabilities and mixing/entrainment is expected. To estimate the importance of this effect we apply a Richardson-number, Ri , criterion. The shear u/h is assumed the same in both layers, but the stratification (density change from lower to upper points) are different, and hence two Ri numbers, with subscripts L and U, are relevant. For both layers, the most unstable domain is expected at the nose where, in dimensional values, $(u^2/h) = (Fr\Psi)^2 U^2/h_0$. Under the assumptions of the model, as detailed in [1], we obtain

$$Ri_L = \sigma \{ Fr^2 H_L [1 - \sigma(1 - H_L)] \}^{-1}, \quad (22a)$$

$$Ri_U = (1 - \sigma) \{ Fr^2 (1 - H_L) [1 - \sigma(1 - H_L)] \}^{-1}, \quad (22b)$$

where $H_L = h_L/h$ at x_N . Here $H_L \approx \Omega^{2/3}$. For a given σ , Ri decreases as Fr increases. During the slumping stage, since Fr is constant, so is also Ri .

The flow is expected to be stable when $Ri > 0.25$, approximately. In the present case of internal stratification, instability may appear in one layer while the other layer is still stable. As explained in [15], an instability in the

lower layer has a mild effect on the propagation: it occurs when $\rho_L \approx \rho_U$, and hence the mixing in this layer will not change much the driving effect due to contrast with ρ_a . However, instabilities in the upper layer, $Ri_U < 0.25$, will mix ρ_U with ρ_a , and practically leave a current of one layer of density ρ_L . This is incompatible with the present model. In our experiments the upper layer was stable, according to both prediction and observation.

3. The experimental layout and procedures

We ran a series of experiments at the Hydraulic Laboratory of the University of Parma.

Our experimental set-up is sketched in figure 2 and consists of a polymethyl-methacrylate channel with a circular cross-section of radius $R = 9.5$ cm. For most experiments, the lock is 102 cm long (reduced to 38 and 20 cm for experiments 39 and 40, respectively, in order to increase the effective Reynolds number), while the downstream channel is 610 cm long. Notice that both the experiments with the reduced lock refer to partial-depth configuration. The lock is separated from the channel by a stainless steel gate, 0.1 cm thick, manually lowered in less than 0.4 s. When the gate is completely open, it closes a micro-switch which turns on an LED in the field of view of a video camera in order to trigger the starting time of the spreading of the current. The video camera is used to estimate the front position as a function of time (a Canon Legria HF 20 full HD video camera, 1920 pixels \times 1080 pixels, working at 25 frames per second (fps)). An operator records the advancing position of the front of the current, observed through a mirror at the bottom of the channel, and measured in metric coordinates by means of a 1 cm grid attached at the bottom of the channel itself. The resolution of the video camera is better than 0.005 cm/pixel.

The lock is initially filled with a two-layer stratification, with the two layers having the same depth $h_L = h_U = R/2$ in full depth configuration (the subscripts L and U refer to the lower and upper layer, respectively). Both layers contain tap water added with sodium chloride (NaCl) and aniline dye, with the upper red (or yellow) layer with density ρ_U which is lighter than the lower blue layer, with density ρ_L , as sketched in figure 2a. For some experiments requiring higher density of the lower fluid, dipotassium phosphate (K_2HPO_4) added to tap water was used, to reach a maximum density $\rho \leq 1.710$ g cm $^{-3}$. The ambient fluid that fills the downstream channel is softened tap water, with density $\rho_a = 1000$ kg m $^{-3}$, as sketched in

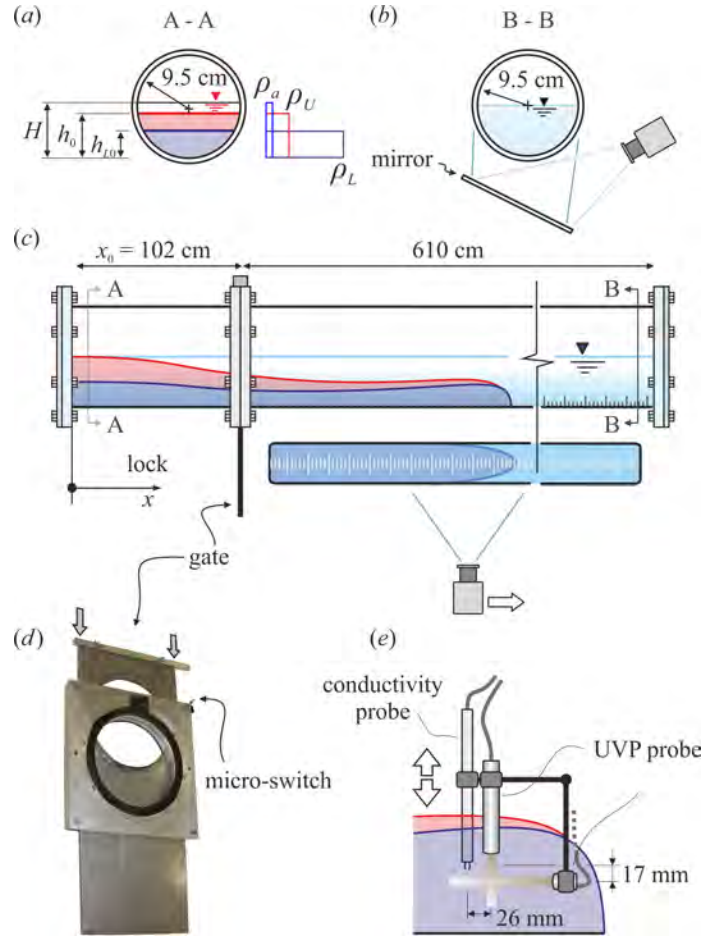


Figure 2: Experimental set-up.

figure 2b. The height of the ambient fluid is the radius, $H = R$. The height of the dense fluid in the lock is the same (full-depth release) or smaller (part-depth release). Several experiments were run with different values of the internal stratification parameter in the lock, $\sigma = (\rho_L - \rho_U)/(\rho_L - \rho_a)$. In partial depth configuration, three layers fill the lock, with the most upper layer of softened tap water.

In all the experiments the main measured variable is the front position as a function of time. In some of the experiments, at $x = 80$ cm from the gate, we recorded the time series of the vertical density profiles of the current by means of a home-made conductivity probe connected to a Conduino device [17],

already successfully used in buoyancy flux experiments [18, 4]. Prior to each experiment, the probe was calibrated using 5 – 6 samples of different known salt content. During these experiments, the conductivity probe moves up and down continuously in time, profiling the density of the fluid from $z = 0$ cm to $z = 6$ cm in approximately 5 s. The vertical velocity of the probe was adjusted to be fast enough to record a quasi-instantaneous vertical density profile, but not so fast to enhance mixing between the dense fluid and the ambient, altering significantly the density field. In some other experiments, the conductivity probe was kept at a fixed position during the test, and the same experiment was re-run in order to have density time series at different levels, typically at $z = 21 - 37 - 45$ mm from the bottom of the channel.

For some experiments the velocity of the dense fluid current was measured in the mid-plane of the cross-section by two Ultrasound Velocity Profilers (UVP, model DOP 2000 Signal-Processing S.A., Switzerland, 2005), in order to acquire data as close as possible to the conductivity probe. One UVP is aligned in the vertical direction, the other one in the horizontal direction, along the longitudinal axis of the channel, as illustrated in figure 2e. To prevent any interference between the conductivity probe and the UVPs, the probes were offset by a few millimetres in the cross direction of the channel. In the adopted configuration, the UVP acquires the velocity in 64 volumes of measurements with a spatial resolution of 0.075 cm (along the axis of the probe) and with a data rate of ≈ 60 Hz (number of profiles acquired per second). See Longo [19] for more details on the instrument and on its applications. The ambient fluid was seeded with TiO_2 particles acting as tracers

The lateral view of the experiments was recorded by two full HD video cameras ($1920 \text{ pixels} \times 1080 \text{ pixels}$, iPhone, Apple Inc.), both working at 30 frames per second (fps). Each camera has a field of view of approximately 1 m along the horizontal direction. A grid with 5 cm horizontally spaced, and 4 cm vertically spaced lines was attached on the external circular wall of the channel in order to mark the lateral profiles of the current in time and to convert the pixel position into metric coordinates, using cylindrical correction and specific proprietary Matlab codes. After extracting the frames from the video by means of a commercial software, it is also possible to plot a time series of a vertical line of pixels corresponding to a specific distance from the lock and show the time evolution of the thickness of the lower layer, upper layer and top mixing region.

3.1. The uncertainty in variables and parameters

The density of the ambient fluid (tap water) and of the dense fluid (salt added water plus aniline) were measured by hydrometers with an uncertainty of 10^{-3} g cm $^{-3}$. The corresponding uncertainty for the parameter $\epsilon = (\rho_L - \rho_0) / \rho_0$ is $\Delta\epsilon/\epsilon = 0.2\%$. The same uncertainty holds for the reduced gravity g' . The instantaneous mass density of the fluid measured with a conductivity probe upon calibration, had an overall accuracy of $\pm 3 \cdot 10^{-3}$ g cm $^{-3}$.

The level of the dense fluid in the lock and the level of the ambient fluid were measured by a ruler with an accuracy of 0.1 cm wrapped around the external wall of the channel. The corresponding uncertainty can be assumed equal to 0.1 cm.

The Reynolds number of the current has an uncertainty $\Delta Re/Re \leq 11\%$, also based on the assumption of an uncertainty of 1% in estimating the kinematic viscosity of salty water.

The front position was detected with an absolute uncertainty of 0.5 cm at a time affected by an uncertainty equal to $0.5/30 \approx 0.02$ s for the video frames. The front speed was computed by fitting a line to the experimental time series of front position with the maximum likelihood method, and by computing the uncertainty of the parameter of the line inclination (i.e., the front speed), with a maximum expected relative uncertainty $\leq 2\%$ (including the uncertainty of the experimental points). The velocity scale had an uncertainty $\Delta U/U \leq 0.4\%$ and the time scale had an uncertainty equal to $\Delta T/T \leq 1.4\%$.

The velocity measured by the UVP had an uncertainty of 4% of the measured value, with a minimum of 0.3 cm s $^{-1}$, see Longo et al. [20].

An absolute uncertainty of 0.1 cm was associated with the vertical position where the measurement of the horizontal velocity is made.

4. The experiments

4.1. Experiments for full depth

Forty experiments were performed, thirty in full depth and ten in partial depth configuration, respectively. Table 1 lists the parameters of the experiments in full depth configuration, $H = h_0$.

Figure 3 shows a sequence of frames for Exp 3, where there is a long portion of the current behind the nose without a distinction of the two layers. A better view of the vertical structure of the current is observed in figure 4

| # | ρ_L (kg m ⁻³) | ρ_U (kg m ⁻³) | g' (m s ⁻²) | σ | U (m s ⁻¹) | T (s) | β_{exp} | Re ($\times 10^3$) |
|-----------------|-----------------------------------|-----------------------------------|------------------------------|----------|-----------------------------|------------|---------------|---------------------------|
| 1 | 1060 | 1023 | 0.59 | 0.62 | 0.166 | 6.17 | 0.812 | 15.7 |
| 2 | 1060 | 1023 | 0.59 | 0.62 | 0.166 | 6.17 | 0.803 | 15.7 |
| 3 | 1062 | 1025 | 0.61 | 0.60 | 0.171 | 5.97 | 0.887 | 16.3 |
| 4 | 1062 | 1025 | 0.61 | 0.60 | 0.171 | 5.97 | 0.814 | 16.3 |
| 5 | 1093 | 1023 | 0.91 | 0.75 | 0.181 | 5.64 | 0.807 | 17.2 |
| 6 | 1095 | 1024 | 0.93 | 0.75 | 0.184 | 5.55 | 0.790 | 17.5 |
| 7 | 1100 | 1050 | 0.98 | 0.50 | 0.234 | 4.37 | 0.940 | 22.2 |
| 8 | 1120 | 1062 | 1.18 | 0.48 | 0.259 | 3.94 | 0.841 | 24.6 |
| 9 | 1119 | 1060 | 1.17 | 0.50 | 0.256 | 4.00 | - | 24.3 |
| 10 | 1040 | 1020 | 0.39 | 0.50 | 0.148 | 6.91 | - | 14.1 |
| 11 | 1036 | 1020 | 0.35 | 0.44 | 0.146 | 7.02 | 0.847 | 13.8 |
| 12 | 1043 | 1020 | 0.42 | 0.53 | 0.150 | 6.84 | 0.833 | 14.2 |
| 13 | 1057 | 1026 | 0.56 | 0.54 | 0.171 | 5.98 | 0.832 | 16.3 |
| 14 | 1045 | 1018 | 0.44 | 0.60 | 0.146 | 7.03 | 0.817 | 13.8 |
| 15 | 1052 | 1022 | 0.51 | 0.58 | 0.159 | 6.42 | 0.822 | 15.1 |
| 16 ^a | 1053 | 1023 | 0.52 | 0.57 | 0.162 | 6.30 | 0.887 | 15.4 |
| 17 ^a | 1054 | 1023 | 0.53 | 0.57 | 0.163 | 6.28 | 0.835 | 15.5 |
| 18 ^a | 1052 | 1021 | 0.51 | 0.60 | 0.157 | 6.52 | 0.820 | 14.9 |
| 19 ^b | 1052 | 1035 | 0.51 | 0.33 | 0.188 | 5.44 | 0.923 | 17.9 |
| 20 ^b | 1052 | 1032 | 0.51 | 0.38 | 0.182 | 5.62 | 0.908 | 17.3 |
| 21 ^b | 1052 | 1035 | 0.51 | 0.33 | 0.188 | 5.44 | 0.904 | 17.9 |
| 22 | 1053 | 1014 | 0.52 | 0.74 | 0.139 | 7.34 | 0.808 | 13.2 |
| 23 ^c | 1054 | 1015 | 0.53 | 0.72 | 0.143 | 7.17 | 0.842 | 13.6 |
| 24 ^c | 1054 | 1015 | 0.53 | 0.72 | 0.143 | 7.17 | 0.820 | 13.6 |
| 25 ^c | 1054 | 1014 | 0.53 | 0.74 | 0.140 | 7.31 | 0.822 | 13.3 |
| 26 | 1051 | 1041 | 0.50 | 0.20 | 0.200 | 5.13 | 0.967 | 19.0 |
| 27 | 1041 | 1041 | 0.40 | 0 | 0.195 | 5.23 | - | 18.6 |
| 28 | 1041 | 1041 | 0.40 | 0 | 0.195 | 5.23 | 0.930 | 18.6 |
| 29 | 1041 | 1041 | 0.40 | 0 | 0.195 | 5.23 | 0.923 | 18.6 |
| 30 | 1041 | 1041 | 0.40 | 0 | 0.195 | 5.23 | 0.954 | 18.6 |

Table 1: List of the experiments and main parameters, full depth. ρ_U and ρ_L are the density of the upper and lower layer, g' is the reduced gravity, $\sigma = (\rho_L - \rho_U)/(\rho_L - \rho_a)$ is the internal stratification parameter, $\gamma(h_0) = 1 - \Omega^2 f(h)/f(h_L)$ with $\Omega = A(h_L)/A(h)$, β_{exp} is the experimental time exponent of the front position in the asymptotic regime, where $x_N \propto t^\beta$, U and T are the velocity and the time scales, respectively, and Re is the Reynolds number. Expts 27-30 are without stratification, for testing the overall behaviour of the current. The superscript a, b, c indicates the experiments for the three series with different σ where measurements of local instantaneous density and velocity was systematically performed at three different distances from the bottom. All the experiments are with $x_0 = 102.3$ cm, $H \equiv h_0 = 9.5$ cm, $h_{L0} = h_0/2$, $\gamma(h_0) = 0.822$, $\Omega = 0.391$.

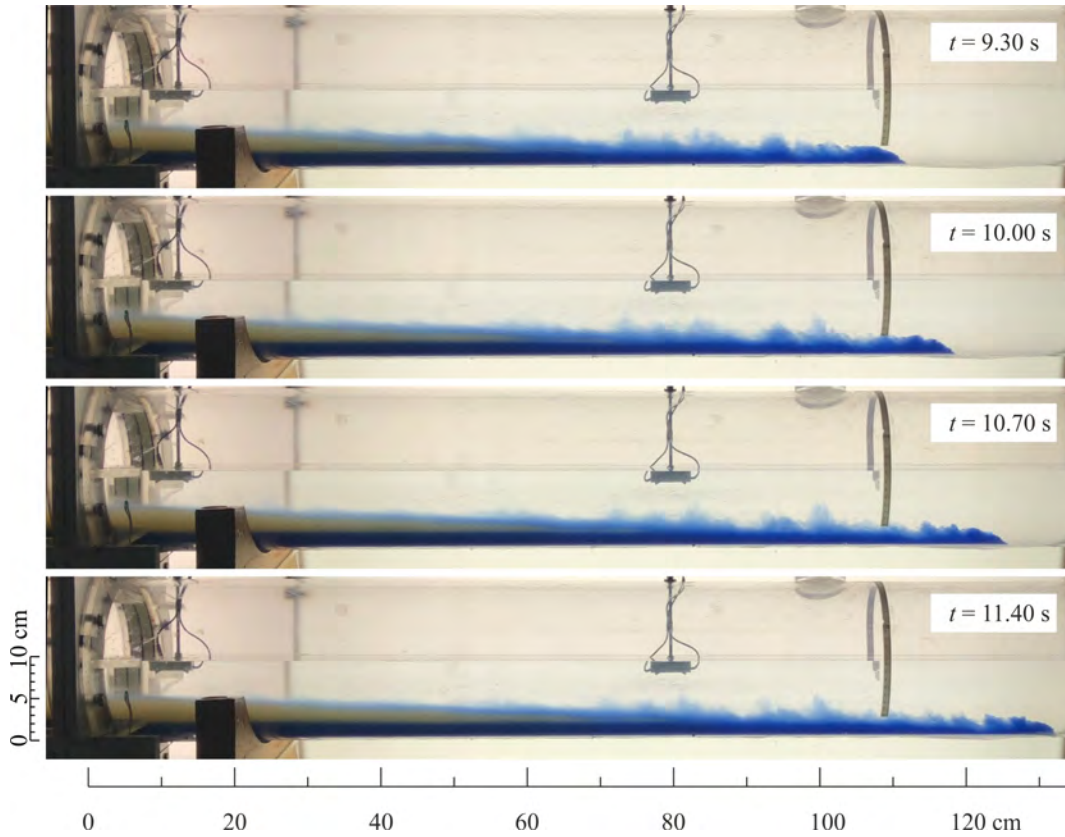


Figure 3: Sequence of frames for Exp 3, the first frame a $t = 9.3$ s, time interval between frames equal to 0.7 s. The boxes in the upper-right corner of each frame show the time elapsed since the gate was opened. Notice that in this case the upper layer is yellow, since a limited number of tests was performed using a yellow dye instead of the red one.

showing three time series of a vertical line of pixels taken at dimensionless $x = 1.8$ (i.e. ≈ 184 cm), during Expts 19 – 18 – 25 respectively, in order to give an overview of the shape of the current propagating in the circular channel for different values of stratification, $\sigma = 0.33 - 0.60 - 0.74$. The lower layer is blue, the upper layer is red, while the ambient fluid is transparent. Firstly, the lower layer, which is heavier, propagates faster, and reaches the fixed cross-section a few seconds before the top layer. The delay between the bottom and top layer increases from a) to c), being equal to 3.5, 6.7, 10.1 s, respectively so with the increase of the internal stratification, σ ; the front speed is ≈ 14 cm s⁻¹ for Exp. 19 and ≈ 21 cm s⁻¹ for expts 18 and 25, hence the space lag is increasing and equal to ≈ 49 cm, ≈ 140 cm and ≈ 210 cm. The second thing that we can notice is that the interface with the ambient fluid is characterized by a significant mixing. As a matter of fact, above the rounded head, a diluted blue layer develops, as a consequence of the exchange of blue fluid between the bottom layer and the ambient. The ambient firstly encounters and interacts with the blue nose of the heavier current and then, climbs up the bump and returns backwards due to the counter current of the ambient fluid, with mixing enhanced by the strong shear between the ambient fluid and the heavy fluid currents. At the same time, the denser fluid also mixes with the less dense fluid, to a variable extent depending on the value of σ . This top layer and the above mixed layer are also characterized by a series of billows and fluctuations, which become less frequent with the increase of σ . The mixed layer tends to deepen from the front to the rear of the current, where the billows become smaller and smaller in amplitude until they disappear. With the increase of σ , the duration (length) of the body of the current also increases. The density interface between the two layers of the stratified current remains always quite sharp. Inside the main body, the interface between the dense and the light fluids appears as a thick dark purple layer as a result of mixing between the red and blue colours, and eventually it becomes thinner and thinner in the tail. The rear of the current has a thinner height than the initial bump, and each of the two layers maintains a nearly constant depth with time.

In the upper part of the figures, some dark shadows can be seen, which are the reflections of the coloured current on the upper free surface.

Contouring the time series gives the interface of the three fluids. In figure 5 we compare the experimental time evolution of the non dimensional height of the upper layer, h_U , (red symbols) and lower layer, h_L , (blue symbols) with the model predictions (solid lines), for Exp 26, with $\sigma = 0.2$ in the

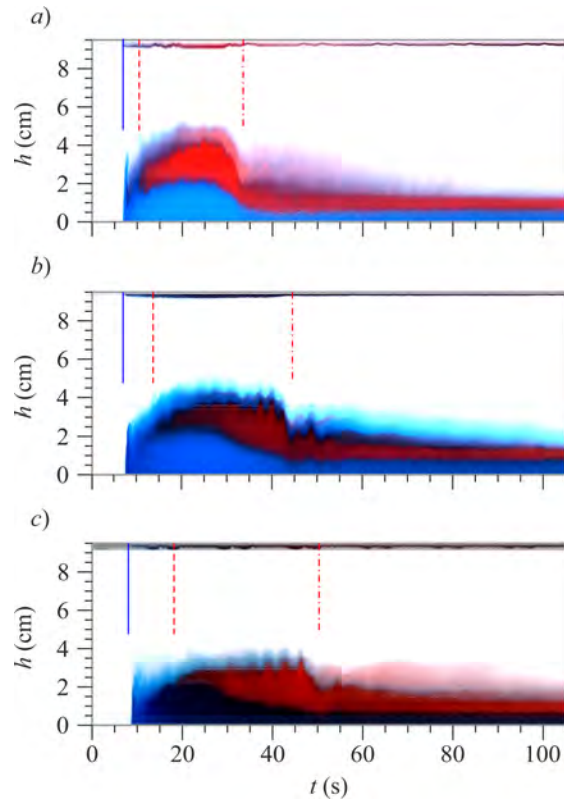


Figure 4: Time series of a vertical line of pixels taken at $x = 1.8$ during Exp. 19 – 18 – 25, with stratification $\sigma = 0.33 - 0.60 - 0.74$ respectively. The vertical black continuous and red dashed and dash-dotted lines mark the front of the heavy fluid current, the front of the light fluid current, the end of the main body of the current.

left panels, and Exp 18 with $\sigma = 0.6$ in the right panels. Generally speaking, the experiments and model agree fairly well for $t > 8$, when both layers decrease in thickness and the long tail of the current develops. The agreement is stronger for higher initial stratification in the lock, i.e. $\sigma = 0.6$. On the other hand, some differences can be seen in the initial phase, for $t < 8$. First of all, the model predicts a localised jump, whereas experimentally the current manifests as a rounded wedge, with a height increasing from $h = 0$ to a crest that is greater than that predicted by the model. In our experiments, we recorded videos only in sections beyond the slumping length, where the theoretical model predicts only a decrease of h after the appearance of the jump, so the current should become thinner everywhere.

In addition, billows and fluctuations of the surface of the current are not captured by the model, which in its simplified form does not consider fluid exchange between the current and the ambient.

The colours only give a semi-quantitative indication of the density, whereas a more accurate estimate can be obtained by direct measurements with the Conduino. Figure 6a-b illustrates the time series of the density profiles of the current, at $x = 1.8$ as a function of height, for Exp 23 ($\sigma = 0.72$) and 11 ($\sigma = 0.54$). The time $t = 0$ s is set at the lift of the gate, while the conductivity probe starts measuring the density as soon as the current approaches the probe. We can see that in both the two experiments, the lower dense layer forms a bump of thickness approximately equal to 2 cm and this bumps persists for a longer time if the stratification of the current is lower. In fact, in figure 6a the bump appears at $t \approx 10$ s and it vanishes at $t \approx 30$ s, while in figure 6b the bump appears at $t \approx 13$ s and it vanishes at $t \approx 45$ s. On the other side, the upper lighter layer forms a rounded wedge which is delayed with respect from the bottom bump in case of strong stratification. In figure 6a, the upper layers reaches a maximum height at $t \approx 35$ s, when the bottom bump has a minimum thickness, while in figure 6b, the bottom and top bumps appear almost synchronized.

The water of the ambient fluid remains fresh far from the current. However, close to the upper layer, different fades of blue in the vertical direction represent some mixing between the current and the ambient.

In both the experiments the current takes almost 70 seconds to reach the end of the channel, when the current becomes a thin constant layer in the whole channel.

Figure 7 illustrates the advancement of the front position, x_N , with time, t , for all the experiments, while the solid black lines refer to the model solu-

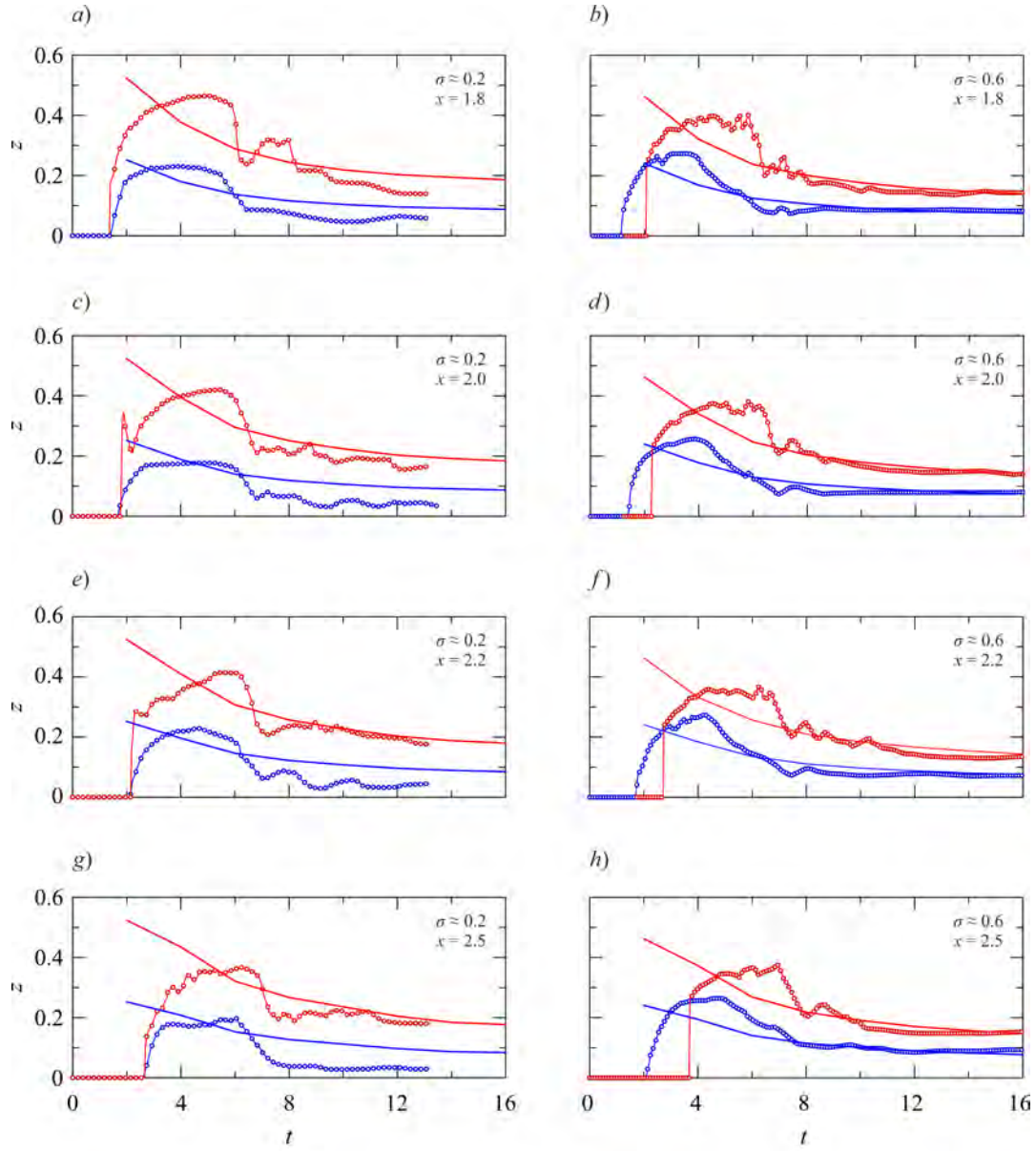


Figure 5: Time evolution of the top limit of the upper layer, h , in red, and of the lower layer, h_L in blue, at $x = 1.8 - 2.0 - 2.2 - 2.5$, for Exp 26 (panels a-c-e-g) and Exp 18 (panels b-d-f-h) of table 1.

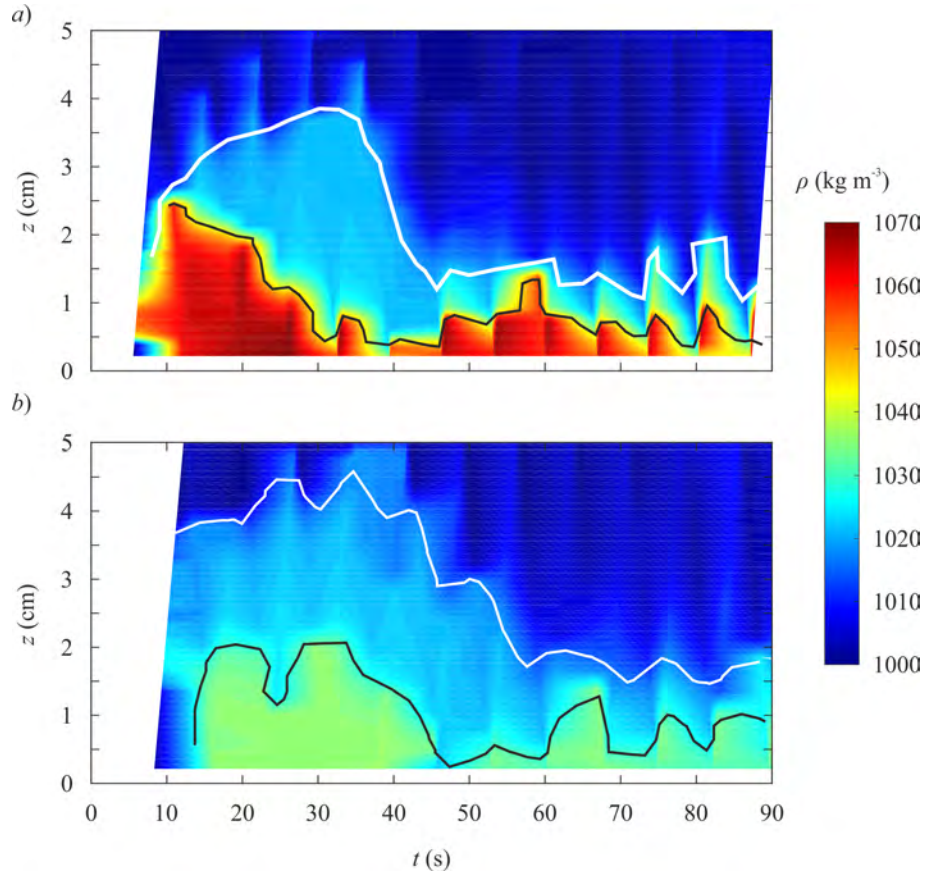


Figure 6: Density measurements at $x = 1.8$ shown in false colour as a function of time and height. *a)* Experiment 23, and *b)* experiment 11. The black line marks the height of the bottom layer, while the white line marks the height of the top layer.

tions. The experiments are separated into seven groups, upon their value of σ , for an easy visualization, with the data groups subjected to a shift in the vertical direction.

For all the experiments, the slope of the asymptotic trend appears significantly consistent with the model for the entire path. The red line with a slope $3/4$ represents the theoretical self-similar solution which is adequately representative of the experiments in the “intermediate asymptotics”, that is not too early, not too late, in the spirit of self similarity approach.

In order to gain a deeper insight, the comparison of the front speed during the slumping phase, and of the time exponent of the front position in the late stage are shown in Figure 8. The front speed is obtained by interpolating the front position in the initial stage, when the front condition is due to characteristics propagating from an unperturbed domain in the lock. Figure 8a shows that the general trend of the model is that of an increase in the slumping velocity with σ , which is very well reproduced by the experiments.

The exponents β are obtained by interpolating a power function to the experimental data for $t > 1$. In the experiments with a homogeneous current ($\sigma = 0$), the experimental β is approximately 10% greater than the theoretical value, but for $\sigma > 0.2$, the experimental β generally superposes with the model in the limit of experimental errors, see figure 8b. A reason for the difference in β for low σ may stand in some instabilities that arise in weakly stratified gravity currents, and in the effects of the internal waves absorbing energy due to buoyancy and convecting it inside the body of the current.

The reasonable agreement suggests that the simple model provides reliable information on the flow field, despite neglecting many aspects (like the dynamics and engulfment of the ambient in the current) that are experimentally observed.

Figure 9a-b illustrates the dimensional horizontal, u , and vertical velocity, v , respectively, at $x = 1.8$ as a function of height, for Exp 12 of table 1. We can see that the dense layer, which has a thickness of about 2 cm, has a horizontal velocity of approximately $u \approx 20 \text{ cm s}^{-1}$ in the early stage, but then decelerates in time until $u \approx 8 \text{ cm s}^{-1}$, matching the value of the top light layer, which seems to propagate at a constant velocity, since the beginning. The solid black line represents the zero velocity contour. Inside this region, the velocity has a general negative value. We may attempt to explain this naively using the fact that the current is spreading and thinning. However, the negative vertical velocity can be observed in the nose of the current, not only during the later phase of depth reduction. In addition,

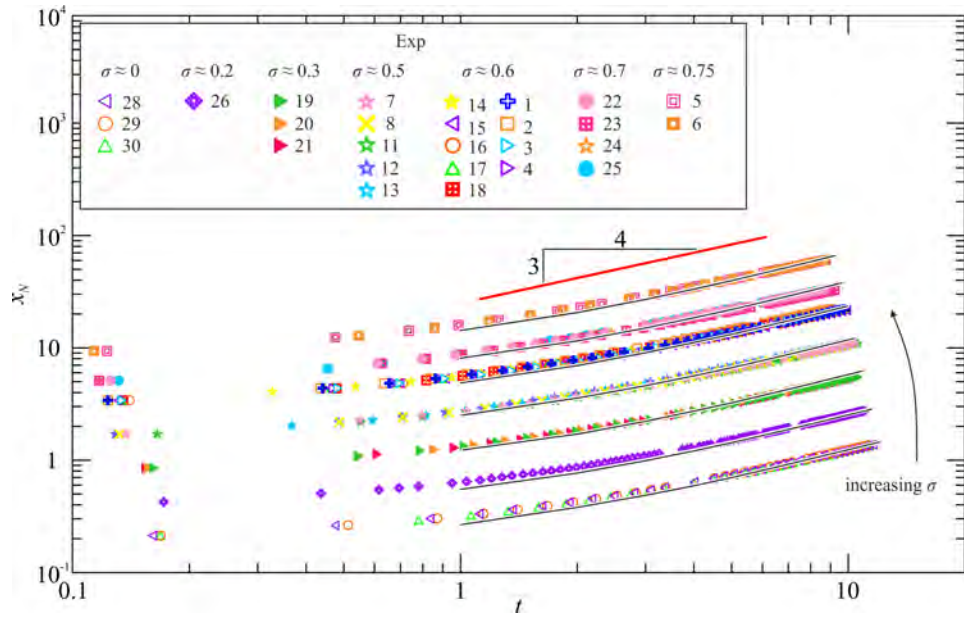


Figure 7: Experimental front position for experiments in full depth, log-log plot. Data have been decimated and for each value of σ are translated in the vertical for an easy visualization. In particular, series with $\sigma < 0.2$ are shifted downward, series with $\sigma > 0.2$ are shifted upward, while series with $\sigma = 0.2$ are unshifted. The solid black lines are the model front positions. The red line represent the expected self-similar solution with a slope $3/4$ as derived from eq.(18).

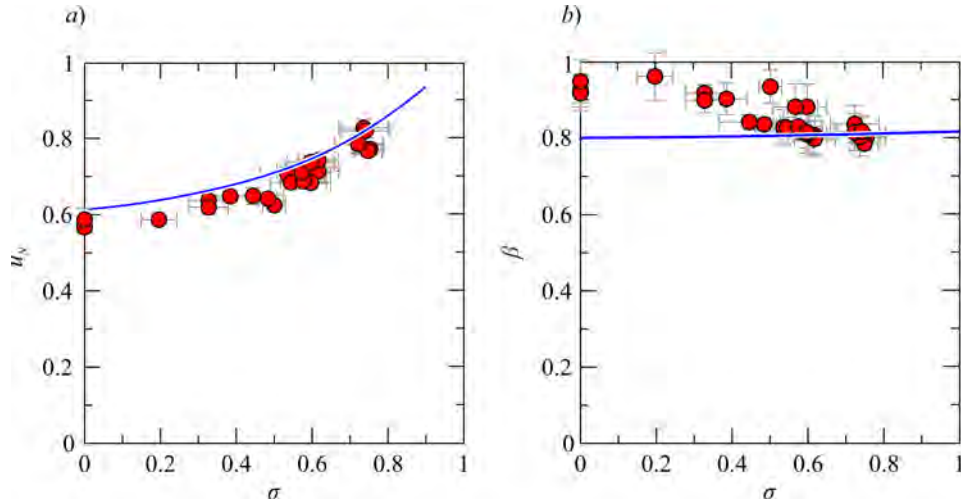


Figure 8: Comparison between experiments and theory. *a)* Slumping phase velocity u_N as a function of σ ; *b)* the exponent β of the front position $x_N \sim t^\beta$ of the intermediate asymptotic self similar solution as a function of the stratification σ . Symbols are experiments, the blue solid line is the model. Error bars refer to two standard deviations.

the values of negative velocity (approximately -2 cm/s) are too high to be only related to the thinning phase of the current, which induces only small negative velocities. Thus, we require another explanation to explain the negative velocities: the ambient fluid is entrained by the current, which becomes increasingly dilute and propagates slower in time.

More detailed local measurements were obtained by keeping the Conduino in a fixed position and continuously recording both the local density and the horizontal and vertical velocity components with the Doppler profilometer. The experiments were repeated by placing the Conduino at a nominal distance of 29, 37, 45 mm from the bottom, with three series of tests distinguished by superscript *a*, *b*, *c* in Table 1 with three different nominal values of σ , for a total of nine tests. In particular, we have considered $\sigma \approx 0.3, 0.6, 0.7$ (test 16-18, 19-21 and 22-25, respectively). We refer to a nominal value of the parameter σ , since sometimes it was non possible to obtain exactly the desired density of the lower/upper layer, and consequently also σ can deviate from the target by a few percentage points. This has no appreciable effect on the present analyses. Figure 10 shows the contours of the timeline in the section of measurements, with the three horizontal lines representing the levels where measurements of fluid velocity and density were simultaneously

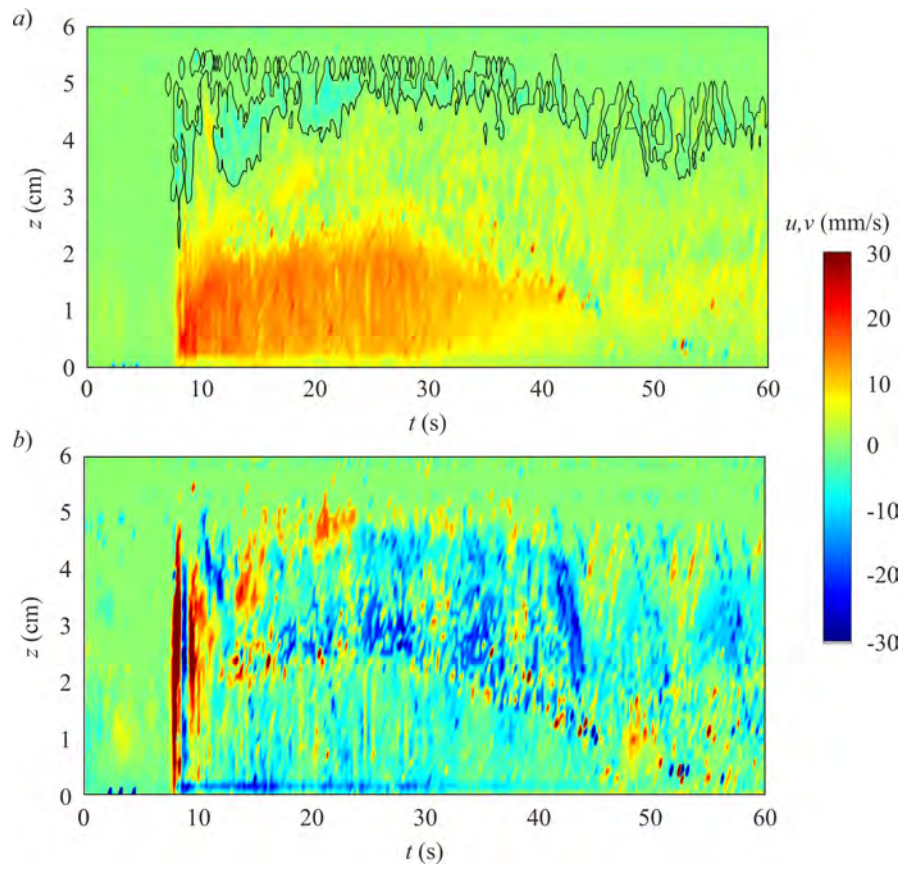


Figure 9: Fluid velocity for Exp 12 measured at $x = 1.8$. a) Horizontal and b) vertical velocity shown in false colour as a function of time and height.

taken. We note that the measurements never refer to the denser, lower layer, while they are temporarily immersed in the upper layer, the mixing region and the ambient fluid.

Raw data were initially subjected to de-spiking [see 21, 22], then low-pass filtered with a cut-off frequency of 0.25 Hz; then, fluctuating components were estimated by difference. In this way, temporal serials were extracted, allowing the reconstruction of vertical and horizontal buoyancy and Reynolds stresses. Figure 11 shows the dimensionless horizontal and vertical velocity, and the Reynolds shear stress at increasing distance from the bottom.

The horizontal velocity profiles in figure 11a-b-c show that the current velocity is highest toward the bottom, with larger values than the front speed in the measurement section (as expected, due to some recirculation of the fluid in the nose), while it is delayed and takes on smaller values in the upper layers. Numerous fluctuations are present, especially at large distances from the bottom where the interaction with the counter-flux of the ambient fluid is relevant. The difference between the maximum horizontal velocity near the bottom and the velocity of the front is reduced by increasing the density contrast σ , and at the same time the non-uniformity on the vertical becomes more marked: a shear in the vertical is evident, with the denser fluid stream near the bottom faster than the less dense one, the more so as σ increases.

The vertical mean velocities in figure 11d-e-f take on much smaller values than the horizontal mean velocity, with a sequence of fluctuations and both positive and negative values. For $\sigma = 0.60$ some very large oscillations are evident in measurements taken near the bottom, presumably due to resonance although no specific analysis has been performed.

Reynolds tangential stresses are calculated as a time average of the instantaneous values, that is

$$\overline{u'v'}(t) = \frac{1}{t} \int_0^t u'(\tau)v'(\tau) d\tau, \quad (23)$$

where u' and v' are the fluctuating velocities and τ is the dummy variable. Figure 11g-h-i shows the profiles of the dimensionless values $\overline{u'v'}$. The lower level always transfers momentum to the layers above, with two peaks at the arrival of the current and the beginning of the decay phase (with the exception of the case $\sigma = 0.70$ for which the second peak is not detected). The upper level, on the other hand, exerts an average negative shear stress.

Figure 12 shows the density measurements and the buoyancy fluxes $\rho'v'$ due to turbulence in the vertical direction.

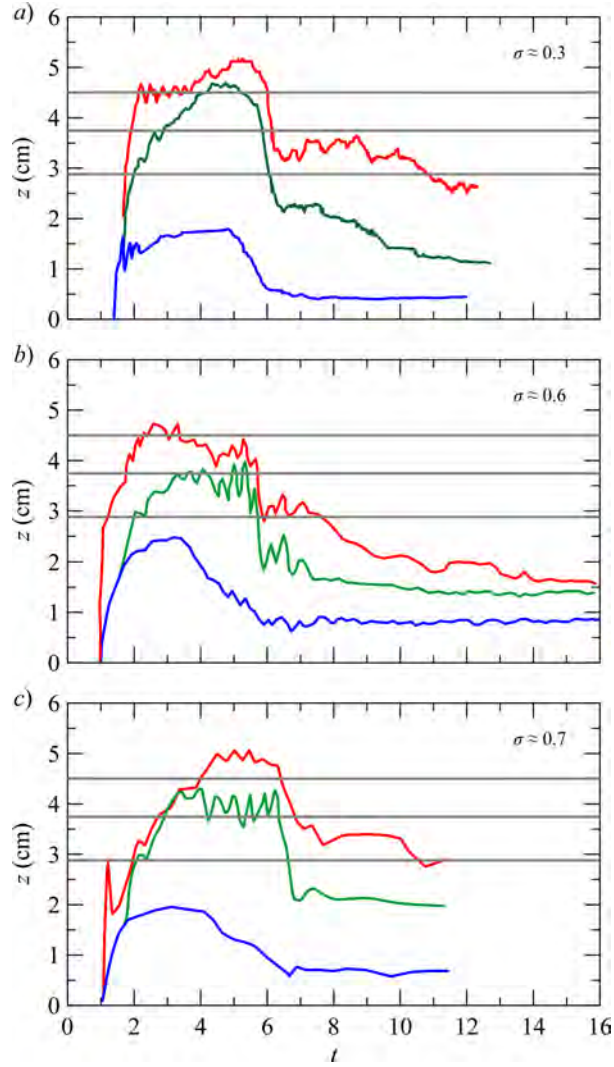


Figure 10: Profiles of the currents in the section $x = 80$ cm where simultaneous measurements of fluid velocity and density were taken. *a)* Profiles for the experiments with $\sigma = 0.33$, *b)* profiles for the experiments with $\sigma = 0.60$, and *c)* profiles for the experiments with $\sigma = 0.70$. The blue curve is the interface between the two layers of the current, the green curve is the interface between the top layer and a mixing zone in the ambient fluid, the red line is the limit of the mixing zone. The three horizontal lines mark the level where velocity and density measurements were taken.

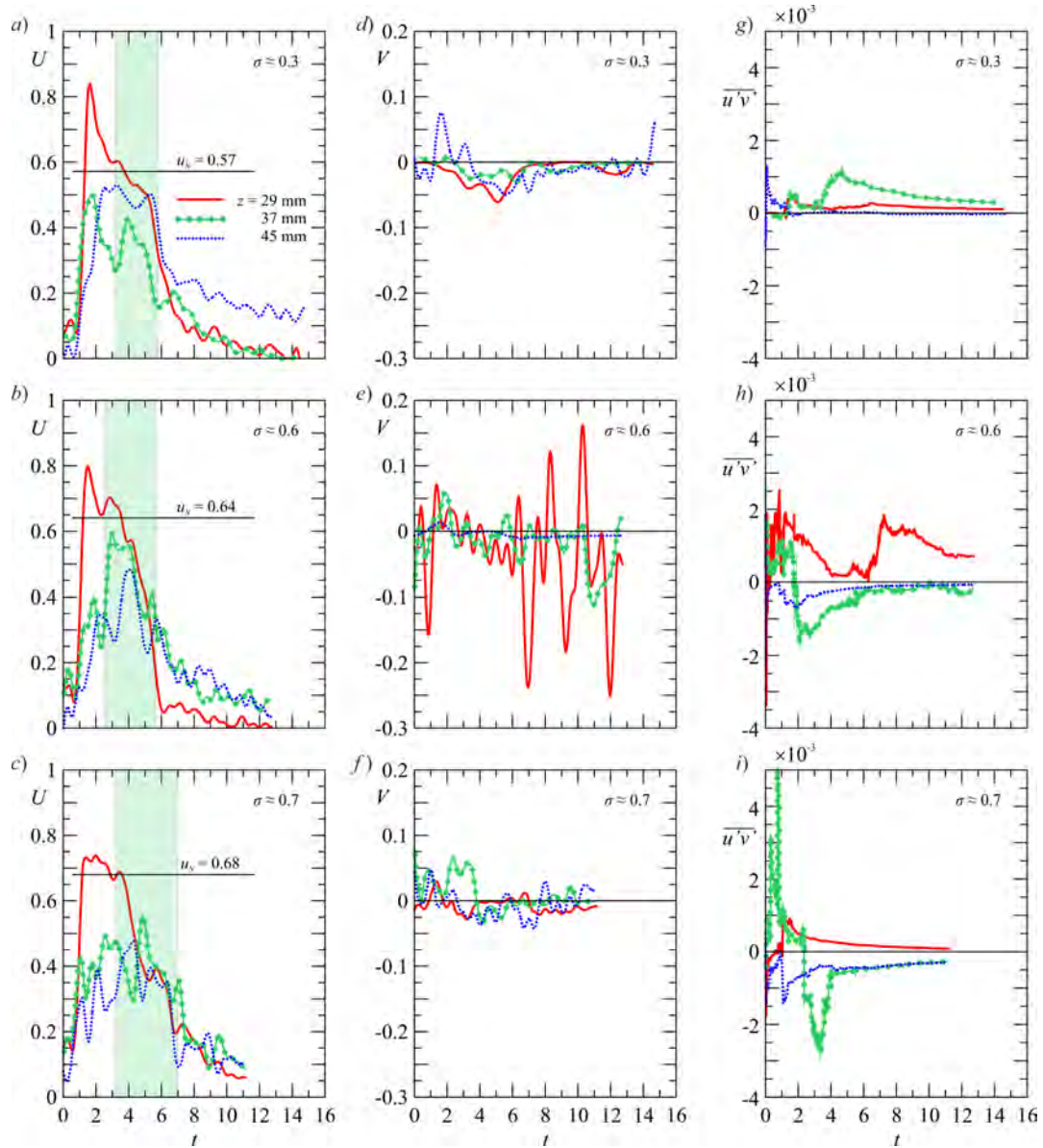


Figure 11: Velocity and turbulence measurements. *a-b-c*) Horizontal, *d-e-f*) vertical velocity, *g-h-i*) Reynolds shear stress for $\sigma = 0.33, 0.60, 0.70$. Measurements are taken at different height from the bottom. $u_N = 0.57, 0.64, 0.68$ is the front speed when the current crosses the section of measurement. The shaded areas indicate the time interval when the interface between the upper layer and the ambient fluid is $z \geq 37$ mm, i.e. when the corresponding probe is immersed in the upper layer.

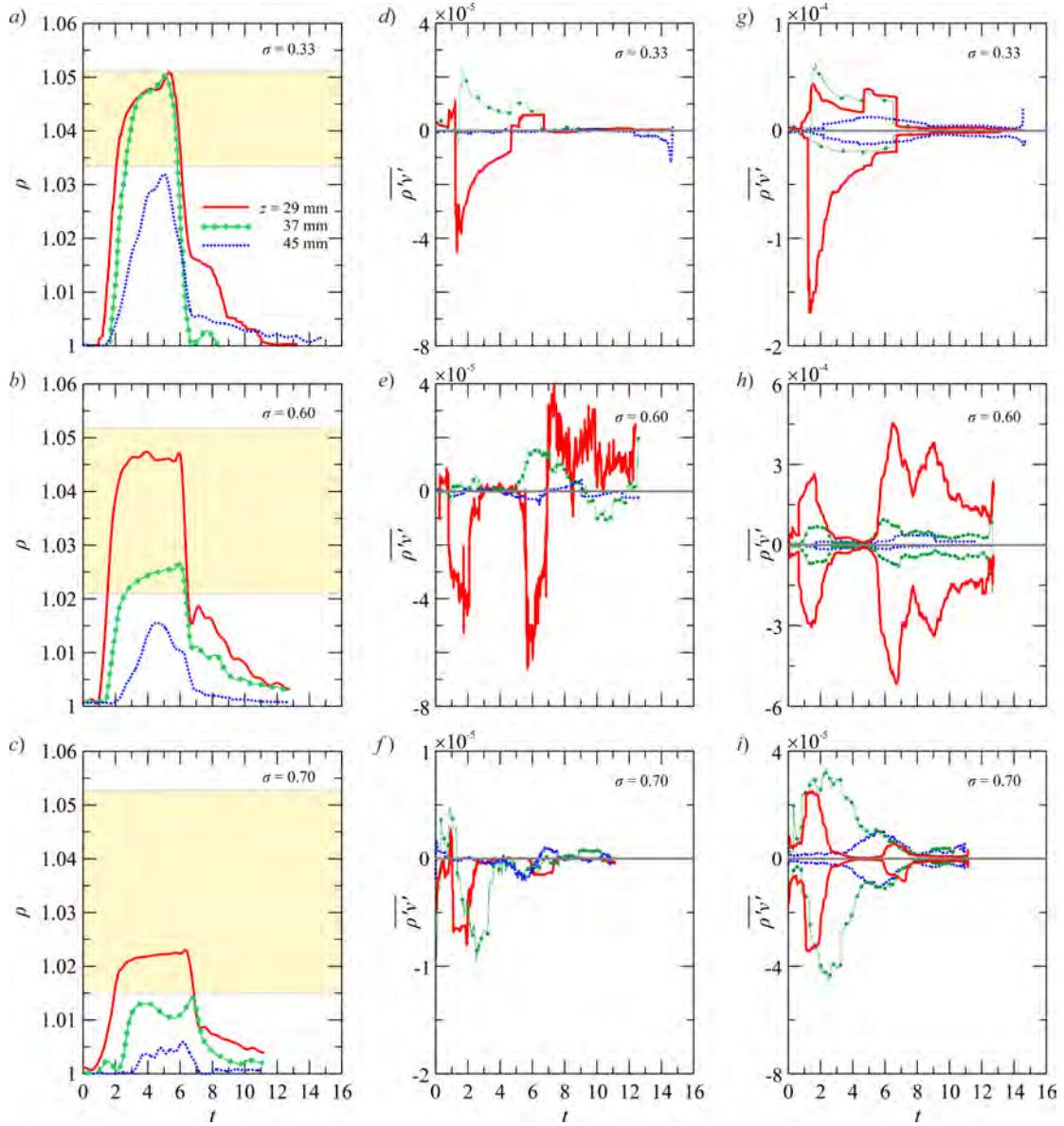


Figure 12: Density and buoyancy fluxes measurements. *a-b-c*) Average density, *d-e-f*) vertical buoyancy fluxes, and *g-h-i*) vertical buoyancy fluxes separated into positive and negative contributions. Test series with $\sigma = 0.33, 0.60, 0.70$ and with measurements taken at different height from the bottom. The shaded areas indicate the domain between the lower layer and the upper layer density.

The profiles should be interpreted bearing in mind that these are Eulerian measurements which, during the propagation of the current, are representative of the dynamics of deeper or shallower layers of the current. Therefore, the signal variation is also due to the time evolution of the current in the measuring section. The average density is clearly affected by the passage of the front and the evolution of the body of the current. As σ increases, the current, at the height of the measurements, appears less dense on average, as a consequence of the lower thickness and a high level of mixing with the ambient fluid. The probe most distant from the bottom is systematically immersed in the ambient fluid or in the mixing layer, as can also be seen in figure 10. A special case is represented by the configuration with $\sigma = 0.33$, in which the probe, although immersed only in the upper layer, records a density equal to that of the denser fluid. This can be attributed to a prominence of the denser current and a three-dimensional structure of the flow field, which is not fully reconstructed on the basis of the side images.

All experiments indicate that the flow intensity due to turbulence is highest at the arrival of the current front and at the depletion phase. Near the bottom the fluxes are generally negative at the arrival of the front, whereas the opposite is true at greater distances from the bottom. Negative buoyancy fluxes transfer buoyancy downwards (i.e. they are due to density fluctuations in excess of the mean being transferred downwards, or to density fluctuations in deficit of the mean invading the upper layers). During the propagation of the body of the current, the buoyancy fluxes are greatly reduced, only to resume when the current exhausts its initial phase, possibly reversed.

Performing the analysis by quadrant (not shown) for the experiments with $\sigma = 0.33$ at the level closest to the bottom ($z = 29$ mm) the negative contributions derive equally from the second ($\rho' < 0, v' > 0$) and the fourth quadrant ($\rho' > 0, v' < 0$), while the positive contributions derive almost completely from the third quadrant ($\rho' < 0, v' < 0$). At the upper level ($z = 37$ mm) the flux is stably positive, with predominant contributions from the third quadrant. At the highest level ($z = 45$, mm) net buoyancy flux is modest, with a substantial balance between all quadrants. The results for the other tests with $\sigma \approx 0.6, 0.7$ are very similar (not shown).

4.2. Experiments for partial depth

Table 2 lists the parameters of ten experiments for partial depth. The experimental front position is shown in figure 13. In the comparisons with the theory, unlike what happens for full-depth experiments, a Froude correction

| # | ρ_L (kg m^{-3}) | ρ_U (kg m^{-3}) | g' (m s^{-2}) | σ | x_0 (cm) | h_0 (cm) | H/h_0 | h_{L0} (cm) | Ω | $\gamma(h_0)$ | U (m s^{-1}) | T (s) | Re ($\times 10^3$) |
|----|------------------------------------|------------------------------------|-------------------------------|----------|---------------|---------------|---------|------------------|----------|---------------|------------------------------|------------|---------------------------|
| 31 | 1040 | 1020 | 0.39 | 0.50 | 102.3 | 6.33 | 1.5 | 3.16 | 0.38 | 0.822 | 0.121 | 8.46 | 7.7 |
| 32 | 1067 | 1020 | 0.66 | 0.70 | 102.3 | 6.33 | 1.5 | 3.16 | 0.38 | 0.822 | 0.133 | 7.71 | 8.4 |
| 33 | 1067 | 1053 | 0.66 | 0.21 | 102.3 | 6.33 | 1.5 | 3.16 | 0.38 | 0.822 | 0.186 | 5.51 | 11.8 |
| 34 | 1039 | 1039 | 0.38 | 0 | 102.3 | 6.33 | 1.5 | 0 | 0 | 1 | 0.156 | 6.57 | 9.9 |
| 35 | 1040 | 1020 | 0.39 | 0.50 | 102.3 | 4.00 | 2.4 | 2.00 | 0.37 | 0.822 | 0.096 | 10.64 | 3.9 |
| 36 | 1067 | 1022 | 0.66 | 0.67 | 102.3 | 4.00 | 2.4 | 2.00 | 0.37 | 0.822 | 0.109 | 9.43 | 4.3 |
| 37 | 1066 | 1053 | 0.65 | 0.20 | 102.3 | 4.00 | 2.4 | 2.00 | 0.37 | 0.822 | 0.147 | 6.95 | 5.9 |
| 38 | 1051 | 1051 | 0.50 | 0 | 102.3 | 4.00 | 2.4 | 0 | 0 | 1 | 0.141 | 7.23 | 5.7 |
| 39 | 1400 | 1200 | 3.92 | 0.50 | 38.0 | 6.30 | 1.5 | 3.16 | 0.38 | 0.822 | 0.382 | 0.99 | 24.2 |
| 40 | 1602 | 1381 | 5.90 | 0.37 | 20.0 | 6.33 | 1.5 | 3.16 | 0.38 | 0.822 | 0.511 | 0.39 | 32.4 |

Table 2: List of the experiments and main parameters, partial depth depth. For caption, see table 1. Expts 34, 35 are without stratification, for testing the overall behaviour of the system. $H = 9.5$ cm for all tests.

has been included with a coefficient χ , as explained in §2. The data show that for all partial-depth cases the ideal theory over-predicts the experiments, and a better agreement is obtained by using a Froude correction coefficient $\chi \in [0.7 - 0.8]$.

Figure 13 also displays the effective Reynolds number of the current, and the Richardson numbers of the lower and upper layers. As far as the stability of the interfaces is concerned, the critical condition is reached at the current front, and the flow is stable if $Ri > 0.25$. This condition is satisfied for practically all tests, both for the upper and lower layers. The minimum value, close to instability, is recorded only for the upper layer in Exp 40.

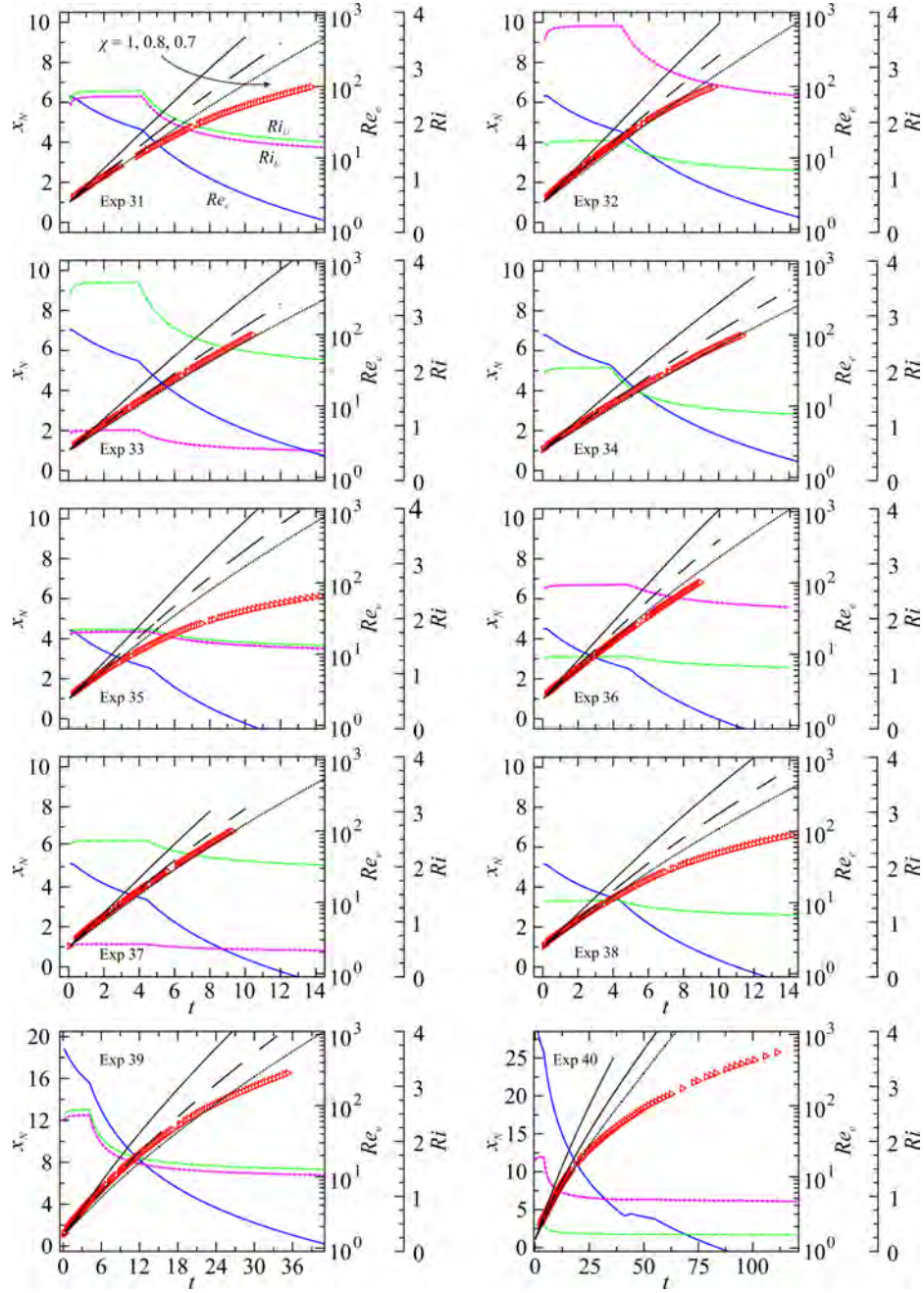


Figure 13: Experimental front position for experiments in partial depth. Symbols are the measurements, continuous, dashed and dotted black curves are the theory with $\chi = 1, 0.8, 0.7$, the blue curve is the effective Reynolds number and the green and magenta curves are the Richardson number for the upper layer and the ambient fluid, and for the lower layer and the upper layer, respectively. For Expts 34, 40 the curve for Ri_L is missing since the current is homogeneous.

5. Conclusion

We experimentally studied the propagation of a lock-release gravity current with an internal stratification in a channel with a circular cross-section. Zemach and Ungarish [15] formulated a one layer approximate model based on shallow water equation, but an experimental validation was necessary in order to assess the accuracy and extend the applicability of that model.

First of all, from the comparison between the approximate model and experimental data, we can state that the measurements of the front position x_N as a function of the time t , based on thirty experiments in full depth, show that the value of β of the law $x_N \propto t^\beta$ is fully consistent with the value predicted by the model for $\sigma > 0.2$. When the current is not stratified, i.e. $\sigma = 0$, the experimental value of β is approximately 10% larger than the model. In addition, the speed of the nose of the current in the slumping phase u_N , reproduces the trend of the model within the experimental error bars, as it tends to increase with the initial internal stratification of the current, σ .

As far as the lateral profiles of the current are concerned, the experimental time evolution of the non dimensional height of the upper and lower layers agree fairly well with the model predictions for $t > 8$, when both layers decrease in thickness and the long tail of the current develops. The agreement is stronger for higher initial stratification in the lock. The differences at the early times, i.e. for $t < 8$, are due to the fact that (i) the model predicts a localized front jump, while the experimental gravity current has a rounded wedge, with a height that increases from $h = 0$ up to a crest, and (ii) the model does not take into account any dynamical interaction between the current and the ambient, so it does not reproduce the billows and fluctuations of the surface of the dense current that are experimentally observed.

The comparison for the ten experiments in partial depth configuration shows a less good agreement, which is improved by applying a reduction coefficient $\chi < 1$ for the Froude number at the front condition. This coefficient compensates for the differences between the ideal free-slip head for which the theoretical Fr was derived, and the realistic front domain (over no-slip boundary and prone to small instability and mixing vortices). The use of $\chi = 0.7 - 0.8$ yields good agreement for several tests. In some other tests, the solution for the late times differs from the experiments, although the correct overlap at least in the early and intermediate times is considered a success for a model with practically no adjustable parameters. The reason for the discrepancies lies in a combination of deliberately neglected effects in

the model. These effects could be included, but their parametrisation is still a challenge.

As an important conclusion of this comparison between theory and experiments, we observe that the theoretical analysis and model based on shallow water equations provide an accurate description of the flow, with correct scaling. This simplified model, although it does not consider any interaction between the dense current and the ambient, is time saving and ready to be used. DNS solutions may give more reliable results but they are usually time consuming, and may be used as a complementary tool in order to further explore some particular and secondary aspects of the flow.

Further information, which is not available from the present model, is obtained by the experiments, regarding the shape of the lateral profiles of the current, the density and velocity fields. From the time series of a vertical line of pixels extracted from a video of the lateral view of the channel, we saw that a strong mixing occurs between the ambient and the nose of the current. The ambient fluid that encounters the nose of the heavier current, mixes with it and climbs up the bump, returning backwards due to the strong shear between the ambient and the stratified current. So above the rounded wedge of the current, a diluted blue layer develops. In addition, the stratification inside the bump depends on the initial stratification of the current in the lock. In fact, for low values of σ , the temporal delay between the top and bottom layers is modest, and their height is approximately equal inside the bump. However, as σ increases, the temporal delay between the two layers increases, and the stratification inside the bump becomes strongly asymmetric in the vertical direction from the nose to the rear of the bump.

Similar observations were drawn from the density field data, we showed that the bumps of the bottom layer and top layer are delayed if the initial stratification of the current is high, while this delay decreases if the density difference between the layer is low.

The analysis of the buoyancy flux generated by turbulence gives indication on the direction of this flux. The quadrant analysis reveals that, near the bottom, the flux is negative, due to density fluctuations with $\rho' > 0$ propagating towards the bottom with $v' > 0$.

Acknowledgements

The cost of the equipment used for this experimental investigation was partly supported by the University of Parma through the Scientific Instru-

mentation Upgrade Programme 2018. D. P. has been partly supported by the Programme “FIL 2019-Quota Incentivante” of University of Parma and co-sponsored by Fondazione Cariparma.

References

- [1] T. Zemach, M. Ungarish, Gravity currents with internal stratification in channels of non-rectangular cross-section, *European Journal of Mechanics-B/Fluids* 89 (2021) 83–92.
- [2] J. E. Simpson, *Gravity currents: In the environment and the laboratory*, Cambridge University Press, 1999.
- [3] H. E. Huppert, Gravity currents: a personal perspective, *Journal of Fluid Mechanics* 554 (2006) 299.
- [4] F. Addona, L. Chiapponi, R. Archetti, Velocity and density measurements in forced fountains with negative buoyancy, *Physics of Fluids* 33 (2021) 055103.
- [5] M. Ungarish, *Gravity Currents and Intrusions: Analysis and Prediction*, volume 1, World Scientific, 2020.
- [6] J. Hacker, P. F. Linden, S. B. Dalziel, Mixing in lock-release gravity currents, *Dynamics of Atmospheres and Oceans* 24 (1996) 183–195.
- [7] B. Kneller, C. Buckee, The structure and fluid mechanics of turbidity currents: a review of some recent studies and their geological implications, *Sedimentology* 47 (2000) 62–94.
- [8] C. Gladstone, R. S. J. Sparks, The significance of grain-size breaks in turbidites and pyroclastic density current deposits, *Journal of Sedimentary Research* 72 (2002) 182–191.
- [9] A. W. Woods, R. S. J. Sparks, L. J. Ritchie, J. Batey, C. Gladstone, M. I. Bursik, The explosive decompression of a pressurized volcanic dome: the 26 december 1997 collapse and explosion of soufrière hills volcano, montserrat, *Geological Society, London, Memoirs* 21 (2002) 457–465.

- [10] L. Ottolenghi, C. Adduce, R. Inghilesi, V. Armenio, F. Roman, Entrainment and mixing in unsteady gravity currents, *Journal of Hydraulic Research* 54 (2016) 541–557.
- [11] L. Ottolenghi, C. Adduce, F. Roman, V. Armenio, Analysis of the flow in gravity currents propagating up a slope, *Ocean Modelling* 115 (2017) 1–13.
- [12] C. Gladstone, L. J. Ritchie, R. S. J. Sparks, A. W. Woods, An experimental investigation of density-stratified inertial gravity currents, *Sedimentology* 51 (2004) 767–789.
- [13] A. Dai, Experiments on two-layer density-stratified inertial gravity currents, *Physical Review Fluids* 2 (2017) 073802.
- [14] C.-S. Wu, A. Dai, Experiments on two-layer stratified gravity currents in the slumping phase, *Journal of Hydraulic Research* 58 (2020) 831–844.
- [15] T. Zemach, M. Ungarish, A model for the propagation of inertial gravity currents released from a two-layer stratified lock, *Journal of Fluid Mechanics* 903 (2020).
- [16] S. Longo, M. Ungarish, V. Di Federico, L. Chiapponi, A. Maranzoni, The propagation of gravity currents in a circular cross-section channel: experiments and theory, *Journal of Fluid Mechanics* 764 (2015) 513.
- [17] M. Carminati, P. Luzzatto-Fegiz, Conduino: affordable and high-resolution multichannel water conductivity sensor using micro USB connectors, *Sensors and Actuators B: Chemical* 251 (2017) 1034–1041.
- [18] D. Petrolo, S. Longo, Buoyancy transfer in a two-layer system in steady state. Experiments in a Taylor–Couette cell, *Journal of Fluid Mechanics* 896 (2020) A27. doi:10.1017/jfm.2020.362.
- [19] S. Longo, Experiments on turbulence beneath a free surface in a stationary field generated by a crump weir: turbulence structure and correlation with the free surface, *Experiments in Fluids* 50 (2011) 201–215.
- [20] S. Longo, M. Ungarish, V. Di Federico, L. Chiapponi, F. Addona, Gravity currents produced by constant and time varying inflow in a circular cross-section channel: experiments and theory, *Advances in Water Resources* 90 (2016) 10–23.

- [21] D. G. Goring, V. I. Nikora, Despiking acoustic doppler velocimeter data, *Journal of Hydraulic Engineering* 128 (2002) 117–126. doi:10.1061/(ASCE)0733-9429(2002)128:1(117).
- [22] N. Mori, T. Suzuki, S. Kakuno, Noise of acoustic Doppler velocimeter data in bubbly flows, *Journal of Engineering Mechanics* 133 (2007) 122–125.